1
2 # On the More Complex Wavelength Dependency of Airy Isostasy in Icy Shells of Ocean Worlds

3 **Wesley S. Tucker[1] and Andrew J. Dombard[1]**

4 [1]Department of Earth and Environmental Sciences, University of Illinois Chicago, Chicago, IL

5 Corresponding author: Wesley Tucker (wtucke5@uic.edu)

6 **Key Points:**

7 - Distinct behaviors emerge in support of icy shell topography at varying spatial scales.
8 - Ice shell thickness estimates using Airy isostasy are valid at only long wavelengths.

9 **Abstract**

10 The topography of ocean worlds is often used to infer ice shell thicknesses by assuming
11 topography is compensated by a basal root. We systematically test the stability of isostatically
12 compensated topography in ice shells. At short horizontal wavelengths, lithospheric strength can
13 support surface topography, while at long wavelengths, buoyancy forces can support topography
14 at the surface and base of the ice shell over geologic time scales. These behaviors are also seen
15 for Airy isostasy in terrestrial worlds. Contrastingly at intermediate scales, the mechanically
16 weak lower ice shell can inhibit the transfer of buoyancy forces to the surface. Factors such as
17 surface temperature can alter the contribution of lithospheric strength, decreasing the stability of
18 a compensating root. This nuanced understanding of icy shell lithospheres provides crucial
19 insights for interpreting surface features and inferring underlying ice shell thickness, with
20 substantial relevance for upcoming space missions to the Jovian system.

21 **Plain Language Summary**

22 Ocean moons have topography on their surfaces that can be used to estimate the thickness of the
23 capping ice shells. In contrast to rocky worlds, the nature of ice shells prevents traditional
24 approaches from being applied. In this study, we use geophysical models to simulate how
25 topography evolves over geologic time. For small features, the stiffness of the ice crust plays a
26 significant role in supporting topography. For larger features, buoyancy forces, like how an
27 iceberg floats, keep topography stable over long periods. In the lower shell near the underlying
28 ocean, the ice is near its melting temperature, which makes it much weaker than the ice nearer
29 the surface. This weakness can prevent the buoyancy forces from reaching the surface for
30 intermediate scale features. Understanding the dynamics of Airy isostasy in ocean worlds can
31 help interpret data collected from space missions, and further our understanding of these icy
32 satellites.

33 **1 Introduction**

34 　　　　Topography on terrestrial bodies is generally supported by a combination of factors.

35 These include variations in crustal thickness, known as Airy isostasy (Airy, 1855), variations in

36 density, referred to as Pratt isostasy (Pratt, 1855), and the strength of the lithosphere (Turcotte et

37 al., 1981). The extent to which lithospheric strength contributes to topographic support depends

38 on the wavelength of the topography (e.g., Turcotte & Schubert, 2014). For instance, at short

39 wavelengths, the lithosphere can fully support the topographic load, analogous to a bookshelf

40 easily supporting a single book. However, at sufficiently long wavelengths where the load is

41 spread out across a larger area, the rigidity of the lithosphere is reduced, similar to many books

42 on a sagging bookshelf. In this case, the topography is compensated by isostasy.

43 　　　　The concept of surface topography being compensated by an opposing basal topography

44 (i.e., Airy isostasy) is simple and appealing. It enables interpretation of gravity and topography

45 data collected by spacecraft requiring only an assumption about the density. Consequently,

46 researchers have widely used this concept to estimate variations in the thickness of icy shells on
47 ocean worlds within the Jovian and Saturnian systems.

48   These icy satellites display a diverse array of topographic features at various horizontal
49 wavelengths. Airy isostasy has been used to estimate ice shell thickness based on observations of
50 surface features and their respective topographies. Shell thickness estimates are commonly
51 derived from long-wavelength topography (e.g., Čadek et al., 2019b; Nimmo et al., 2011; Schenk
52 & McKinnon, 2009), and are often used as an explanation for unexpected topography
53 observations. For example, the unexpectedly large amplitude of Titan's long-wavelength
54 topography may be explained, in part, by isostatic compensation (Nimmo & Bills, 2010).
55 Estimates based on long-wavelength variations in shell thickness assume that the shell is in a
56 constant state of equilibrium. Effectively, ice flow at the base of the ice shell, driven by
57 horizontal pressure differences, reduces basal topography and the surface moves in lockstep,
58 maintaining a constant compensation (e.g., Ojakangas & Stevenson, 1989; Stevenson, 2000).

59   Short-wavelength features are strewn across the icy surfaces ocean worlds. Europa's
60 surface is most notably characterized by intersecting ridges that can extend for more than 1000
61 km with a relief of ~200 m (e.g., Pappalardo et al., 1999; Prockter & Patterson, 2009).
62 Additionally, dark bands on Europa can rise up to 150 m above the surrounding terrain and span
63 several tens of kilometers (Nimmo et al., 2003b). Although linear features are ubiquitous on
64 Europa, there are also small pits and uplifts with average diameters of around 5 km. Singer et al.
65 (2021) employed a basic Airy isostasy model to estimate a minimum shell thickness for Europa
66 of about 3-8 km, based on the size of these small pits. However, if sufficiently thick, the ice shell
67 likely has the rigidity to support short-wavelength features (e.g., Nimmo et al., 2003a).

68   Ice shell thickness estimates have also been derived from chaos terrain on Europa.
69 Williams & Greeley (1998) estimated a minimum thickness of just 0.2-3 km at Conamara Chaos,
70 based on the interpretation that the blocks of the chaos terrain were floating in a liquid at the time
71 of formation. In addition to the short-wavelength icy blocks, chaos terrains display longer-
72 wavelength topographic signature suggesting a compensated state (e.g., Schenk & Pappalardo,
73 2004; Schmidt et al., 2011).

74   Recently, efforts have been made to refine Airy isostasy for use on ice shells, specifically
75 at low spherical harmonic degrees (see Beuthe 2021a, 2021b for an extensive review).

76   Hemingway and Matsuyama (2017) argued that the traditional form of Airy isostasy, in which

77   columns of equal width contain equal mass, is not applicable when using spherical geometry as it

78   causes lateral pressure gradients. The authors proposed an approach that assumes continuous

79   pressure along internal equipotential surfaces. Čadek et al. (2019a) assessed the accuracy of

80   these two approaches, and an "equal stress approach" proposed by Dahlen (1982), to a numerical

81   solution of viscous flow in the crust. The authors concluded that the equal pressure approach

82   may lead to inaccurate estimates of shell thickness for spherical harmonic degrees $l \leq 10$ when

83   assuming a constant viscosity. When viscosity of the ice was temperature dependent, all models

84   lost accuracy with increasing spherical harmonic degrees.

85   A few researchers have presented models that aimed to explain the support mechanism

86   for observed features on the surface of icy ocean worlds such as the plateaus on Titan

87   (Schurmeier et al., 2016) and the megadome on Ganymede (Kay et al., 2018). For both instances,

88   buoyancy forces were not transferred to the surface, which caused the topography at the surface

89   and at the base of the shell to relax away. The megadome on Ganymede was found to be stable

90   over geologic times only when Pratt isostasy was the assumed mechanism of support. On Titan,

91   the plateaus could not be sustained via Airy isostasy, which implies that these features are

92   unlikely to be the result of crustal thickening.

93   Inherent to the nature of icy shells is the mechanical weakness near the ice-ocean

94   interface. Consequently, a material near its melting point (i.e., the lower ice shell) should be

95   limited in its ability to transfer buoyancy stress to support surface topography. This characteristic

96   injects a level of complexity into the understanding of icy shell topographies and the mechanisms

97   that give rise to their support. In this paper, we explore the mechanics of buoyantly supported

98   topography from short wavelength to hemispheric wavelength scales. With upcoming spacecraft

99   missions such as NASA's Europa Clipper and ESA's JUICE, understanding the dynamics of

100 floating ice shells is crucial for providing a foundation for interpreting the trove of topographic

101 data that could profoundly alter our knowledge of icy ocean worlds.

102 **2 Methods**

103 2.1 Finite element simulations

104 We use the commercially available Hexagon Marc finite element package to test

105 systematically for buoyant support of topography in icy shells. The software is well vetted for

106 investigations of lithospheres of icy shells (e.g., Damptz & Dombard, 2011; Dombard &

107 McKinnon, 2002, 2006a; Kay & Dombard, 2018). The code simulates Maxwell viscoelasticity,

108 capturing the behavior of geologic materials at both short and long timescales, (and while not

109 invoked in our simulations, it can include plasticity as a continuum approximation for brittle

110 failure at large stresses). We test for buoyant support of topography for wavelengths $\lambda = 10$ km

111 up to hemispherical scales (i.e., spherical harmonic degree $l = 2$), increasing logarithmically.

112 Although our study is designed to be applicable to all icy ocean worlds, we use Europa to guide

113 the selection of our model parameters. The full finite element simulation is comprised of two

114 steps. A thermal simulation is run to determine the temperature structure, and the results of the

115 thermal simulation are used in the mechanical simulation.

2.2 Mesh and boundary conditions

117 We utilize planar half space meshes split into two layers: an outer ice shell, modeled to

118 be 20 km thick based on estimates for Europa (e.g., Billings & Kattenhorn, 2005; Hussmann et

119 al., 2002), and an ocean with a boundary far enough away to not affect the solution (see Figure

120 S1 in the supporting information for model schematic). For short wavelengths, the ocean mesh

121 layer is ~2.5 times the wavelength. For long wavelengths ($l \geq 6$), the thickness of the ocean layer

122 is reduced to < 2.5 times the wavelength, because of computational limits for large meshes. The

123 planar meshes we implement do not include support from membrane stresses. Membrane stresses

124 become appreciable when the horizontal scale of a spherical harmonic degree, l, is roughly the

125 same as the value given by $l \approx \sqrt{R/d}$, where R is the planetary radios and d is the lithospheric

126 thickness (Turcotte et al., 1981). For Europa, this corresponds to a spherical harmonic degree of

127 ~16 (~600 km). As will be discussed in subsequent sections, the additional support provided by

128 membrane stress simply adds to the already sufficient support to maintain topography at those

129 wavelengths.

130 Elements in our mesh are uniformly distributed in the ice shell layer. In the ocean layer,

131 elements are more densely packed near the ice-ocean boundary, ensuring a higher resolution in

132 this region, while still adhering to a 4:1 aspect ratio throughout. Mesh resolution is variable

133 depending on the scale of the wavelength. At the smallest scales, the ice portion of the mesh has,

134 at minimum, 400 finite elements (40 in depth and 10 in width). At the largest scales, this ratio is

135 reversed to keep within the 4:1 aspect ratio, with 400 elements in width and 10 in depth.

136   Simulations with increased element density in the ice shell portion of the mesh showed no

137   noticeable differences in the results, confirming that the mesh resolution used is adequate for

138   capturing the key dynamics across all scales. Free-slip conditions are applied to the symmetry

139   boundaries at the sides of the mesh, restricting normal displacements, and the bottom of the mesh

140   is locked horizontally and vertically. On the surface, we place sinusoidal topography with an

141   amplitude h of 100 m for all wavelengths, as wavelength controls buoyant support rather than

142   topographic amplitude (see Turcotte & Schubert, 2014). We simulate two scenarios for initial

143   topography at the base of the ice shell: 1) a flat basal surface (i.e., no initial compensating

144   topography), and 2) a root in isostatic equilibrium. The maximum amplitude of the isostatic root

145   H is determined by the density contrast between the water ice and ocean where

146
$$H = \frac{\rho_i h}{\rho_w - \rho_i}. \tag{1}$$

147   In this equation, the density of the liquid water ρ_w is assumed to be 1000 kg/m^3, while the density

148   of the ice shell ρ_i is 920 kg/m^3. Gravitational body forces are applied uniformly to the mesh with

149   an acceleration equal to 1.315 m/s^2.

150   2.3 Material and thermal properties

151   The elastic parameters for ice include a Young's modulus of 9.32 GPa and a Poisson ratio

152   of 0.325 (Gammon et al., 1983). However, in simulations, applying a gravitational load to a

153   compressible material leads to deviatoric stresses from self-compaction. Following Dombard and

154   McKinnon (2006b), we make the material nearly incompressible by adjusting the Poisson ratio to

155   approach 0.5, while also reducing the Young's modulus to 7.83 GPa as to maintain the flexural

156   rigidity of the ice (Turcotte & Schubert, 2014, equation 3-72). The viscosity structure of the ice

157   layer has the greatest influence on relaxation rates (Dombard & McKinnon, 2006a), and when

158   incompressibility is approximated, the variation is negligible (Dombard et al., 2007).

159   Additionally, we follow the ductile creep laws from Goldsby and Kohlstedt (2001).

160   Several mechanisms affect the viscous flow of ice below the brittle-ductile transition. There are

161   three different dislocation (dis) creep mechanisms with temperature dependent contributions

162   (Durham & Stern, 2001), diffusion (diff) creep; and dislocation in an easy-slip (ES) system and

163   grain boundary sliding (GBS) acting as rate limiters. Thus, the total strain rate is

164
$$\dot{\epsilon}_{total} = \dot{\epsilon}_{dis} + \dot{\epsilon}_{diff} + \left(\frac{1}{\dot{\epsilon}_{ES}} + \frac{1}{\dot{\epsilon}_{GBS}}\right)^{-1}.$$
(2)

165 Each of these strain rates can take the general form

166
$$\dot{\epsilon} = A \left(\frac{1}{d}\right)^{m} \sigma' e^{-\left(\frac{Q}{RT}\right)},$$
(3)

167 where $\dot{\epsilon}$ is the equivalent strain rate, A is a material dependent pre-exponential constant

168 normalized for uniaxial deformation, m is a grain size index relating to the grain size d, Q is the

169 activation energy, R is the universal gas constant, and T is absolute temperature. We assume a

170 grain size of 1 mm (e.g., Dombard & McKinnon, 2006a). The full creep parameters are listed in

171 Durham et al. (2010) and references therein.

172   The thermal conductivity of water ice is temperature dependent, given by $651/T$

173 (Petrenko & Whitworth, 1999). In our steady state thermal simulation, we lock the surface

174 temperature at 100 K and the ice-ocean interface temperature at the melting point of ice, 273 K

175 (q ≈ 32 mW/m^3). Heat flows on Europa might be higher, instigating convection near the base of

176 the shell (e.g., McKinnon, 1999; Tobie et al., 2003). Nonetheless, for our purposes, the situation

177 is mechanically identical: a structurally weak base overlaid by a relatively thinner lithosphere

178 (see below).

179   The water below the ice shell lacks material strength and therefore does not provide

180 resistance; rather, it provides a buoyant restoring force. The viscosity is so low compared to the

181 lithospheric ice in the upper shell that it simply needs to accommodate space for the deforming

182 ice at least as fast as that ice is deforming. Therefore, we set the material properties of the water

183 to be the same as the overlying ice layer, with the exception of the density contrast. We also test

184 for the effects of surface temperature, which have been shown to be a controlling factor in creep

185 rates (e.g., Damptz & Dombard., 2011), and the effects for a reduction in the melting

186 temperature of ice due to the presence of an antifreeze such as ammonia (e.g., Spohn & Schubert,

187 2003). To test for effects of buoyancy, we run the simulations without the density contrast,

188 precluding isostasy. Variations in model parameters are shown in Table S1 in the supporting

189 information.

190   We run the simulations for 3 Gyr, a time more than sufficient to capture any appreciable

191 flow in the lower ice shell. Time steps are controlled by the minimum Maxwell time, which is

192 dependent upon, in part, the viscosity (Turcotte & Schubert, 2014). We limit minimum viscosity

193   in the mesh to 10^{18} Pa s due to computational constraints. While a reduced viscosity cutoff

194   accelerates relaxation (Figure S2 in the supporting information), the core behavior remains

195   consistent.

196   Simulations are performed under full large-strain formulation, which includes a second-

197   order term to strain-displacement relationships (e.g., Ranalli, 1995), and a continual geometric

198   update. Although strains are typically small, the large strain scheme is essential for the geometric

199   update, as without it, stresses would not decay as topography relaxes (e.g., Dombard &

200   McKinnon, 2006a). In addition, we apply constant dilatation across the elements to eliminate

201   potential numerical errors caused by simulating a nearly incompressible material.

3 Results

203   The evolution of topography can be described best by three general wavelength

204   categories: short, intermediate, and long. Figure 1 shows the simulation results for the evolution

205   of topography at the surface and base of the ice shell for three representative wavelengths within

206   these categories.

207   At short wavelengths, the surface topography remains stable over the simulation time

208   regardless of buoyancy. In contrast, the basal topography relaxes away, losing 991 m of its initial

209   amplitude. For intermediate wavelengths, the surface topography relaxes in both the buoyancy

210   and no buoyancy simulations. However, the degree of relaxation is substantially greater when the

211   density contrast is not present. For instance, for a wavelength of 100 km, the surface loses

212   approximately 65% of its elevation over the simulation time, compared to an 85% loss for the

213   no-buoyancy scenario (Figure 1c). The root topography at intermediate wavelengths also relaxes

214   when the density contrast is present. Moreover, the root relaxes at a different rate than the

215   surface topography, leading to a deviation from the expected isostatic equilibrium (Figure 1d).

216   This discrepancy arises from the shared contribution of both lithospheric support and buoyancy

217   (Figure 2a). In the case of long wavelengths, without the density contrast, the surface completely

218   relaxes away in less than 100 kyr. Conversely with the density contrast, the surface and the root

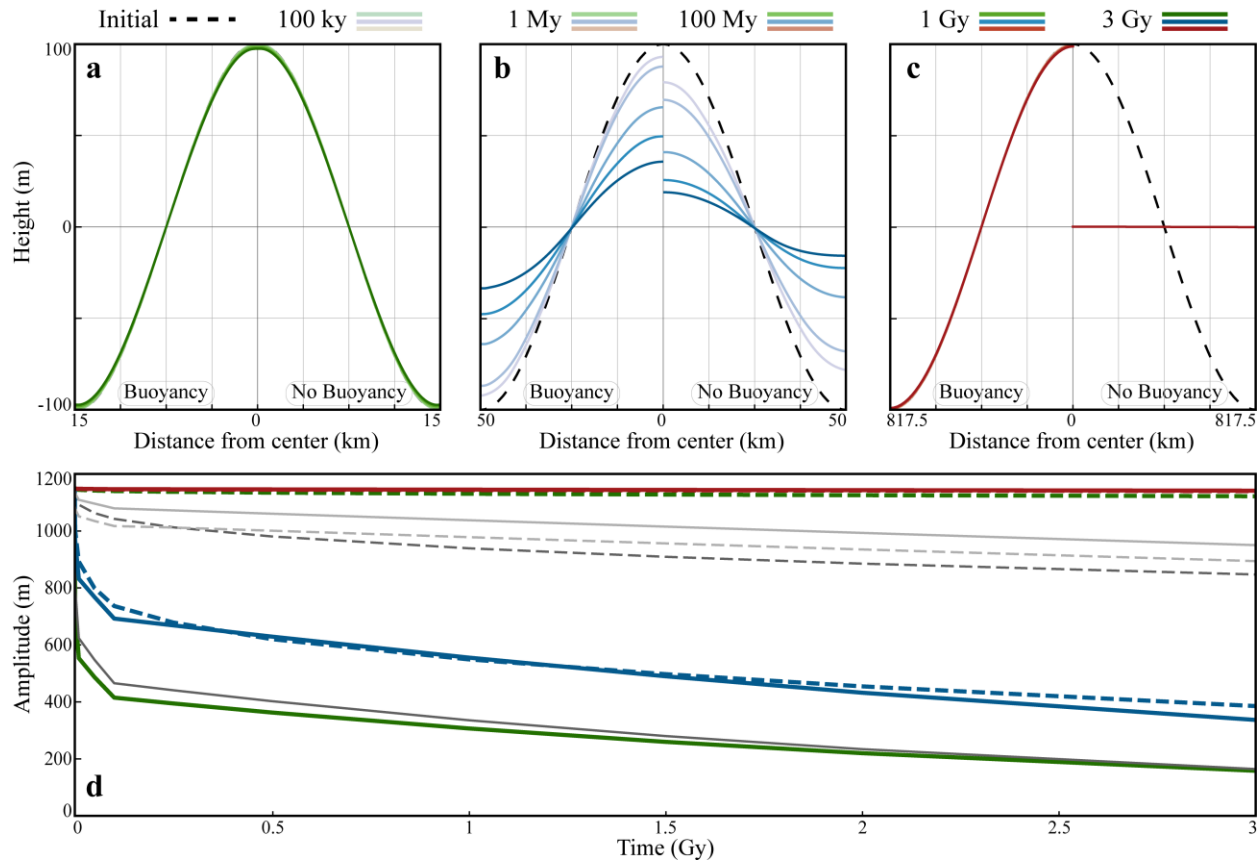219   are stable over geologic times.

Figure 1. (a) 30 km, (b) 100 km, and (c) 1635 km (spherical harmonic degree $l \approx 6$) simulations of surface topography. The initial topography (black dashed line) is consistent across each model with sinusoidal amplitudes of 100 m. The left side of x=0 are simulations with an ice-ocean density contrast (i.e., "Buoyancy"), while the right side are simulations without the density contrast (i.e., "No Buoyancy). The progression of time is indicated by the shade of the color, with lighter shades representing earlier time steps and darker shades indicating later ones. (d) Time series of the amplitude of root topography for the wavelengths presented in (a)–(c). Additionally, root amplitudes for 55 km and 316 km are shown in dark grey and light grey, respectively. For each wavelength, the solid line is the root amplitude of the buoyancy simulation, and the dashed line is the expected root amplitude based on the surface topography of the buoyancy simulation. When the dashed line and solid line are the same, the isostatic equilibrium is maintained.

In Figure 1d, root amplitudes serve as indicators of the varying contribution of lithospheric strength and buoyancy across different wavelengths. At the shortest wavelengths, lithospheric strength dominates, and the root is decoupled from the surface and can flow away. Thus, the predicted root topography, found using equation (1) on the simulated surface topography, remains close to the initial amplitude of 1150 m, while the simulated root topography collapses. As wavelengths reach the intermediate scale, lithospheric strength

239   continues to be the primary support mechanism, but buoyancy begins to contribute. This effect is

240   evident around 100 km wavelength, where the simulated and expected root amplitudes are

241   similar, but their rates of amplitude loss differ, indicating that isostatic equilibrium is not

242   maintained. Beyond these scales, where lithospheric strength becomes less effective, the rate and

243   magnitude of amplitude loss for both the simulated and expected root decreases. Ultimately, at

244   the longest wavelengths, buoyancy becomes the sole support mechanism, and the simulated and

245   expected root are near the initial 1150 m amplitude.

246   Simulations with a surface temperature of 100 K show that the lithosphere supports the

247   topographic load up to wavelengths of ~30 km (Figure 2). Lowering the surface temperature

248   increases the wavelengths at which lithospheric strength can effectively contribute to

249   topographic support. A decreased surface temperature also reduces the degree of relaxation

250   occurring at intermediate wavelengths. For example at 100 km, the simulated surface topography

251   with temperatures of 100 K relax ~65 m, compared to ~15 m when the surface temperature is 70

252   K. A similar effect is observed when the melting temperature (i.e., the temperature at the ice-

253   ocean interface) is reduced to 176 K (Figure 2b). Under these conditions, the contribution of

254   lithospheric support is greater at longer wavelengths, and the maximum topographic relaxation is

255   reduced.

256   At wavelengths < 80 km, the simulations with an initially flat ice shell base are nearly

257   identical to the simulations without the density contrast (Figure 2b). This finding further

258   underscores that lithospheric strength is the primary mechanism of topographic support at short

259   wavelengths. However, at wavelengths greater than 100 km, without an initial compensated root,

260   the surface topography relaxes to just a few meters over the simulated time. At the longest

261   wavelengths, a root forms that is in isostatic equilibrium with the reduced surface topography.
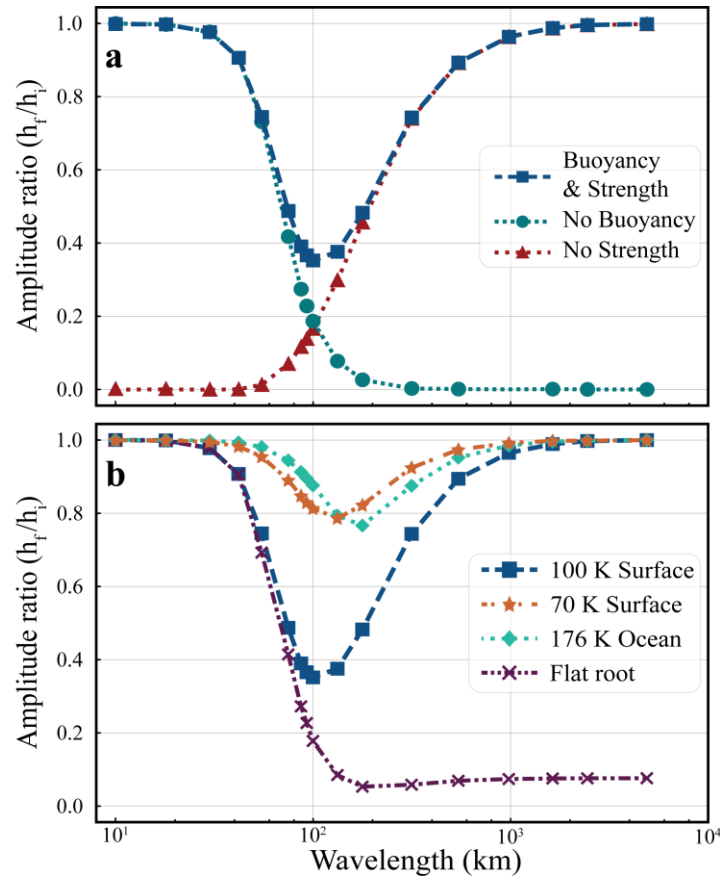
262

Figure 2. Ratio of initial to final topographic amplitude for simulations across simulated wavelengths for (a) simulations with and without buoyancy and (b) variations in the assumed initial state of the temperature at the surface and base of the ice shell. The "No Strength" curve is the difference between "Buoyancy & Strength" and "No Buoyancy." Because the simulations (except the "Flat root" ones) are set up to be in isostatic equilibrium, the ratio should be pegged to a value of 1 if the precepts of Airy isostasy hold; i.e., Airy isostasy fails when the amplitude ratio is < 1. Refer to section 2 and Table S1 in the supporting information for details on the boundary conditions of each simulation type.

4 Discussion

The prevalent assumption that Airy isostasy can be utilized for estimating ice shell thickness does not hold true except at the longest wavelengths. A significant oversight in this assumption lies in the positioning of the lithosphere relative to the ice-ocean boundary. On Earth, the lithospheric boundary is situated beneath the density contrast of the crust-mantle boundary. Thus, when a surface load deforms the lithosphere, both the crust and the upper mantle will respond to the deformation (e.g., Barrell, 1914; Daly, 1940). However, in the case of ice shells, the lithosphere is embedded within the ice itself, because the ice in the lower portion of the shell is approaching its melting point and is therefore weak over geologic time scales. A convective

280   portion in an ice shell that passes a higher heat flux would only exacerbate this effect. Relative to

281   a conductive ice shell, a convective shell of the same total thickness would see higher

282   temperatures at shallower depths, resulting in a thinner lithosphere and a thicker channel that

283   decouples the root topography from the surface, permitting lower crustal flow to longer

284   wavelengths. The thinner lithosphere would shift the "No Buoyancy" (i.e., all lithospheric

285   strength) curves in Figure 2 to the left, while the thicker channel would shift the "No Strength"

286   (i.e., all buoyancy) curves to the right. The combined effects would yield an exacerbated (i.e.,

287   wider) intermediate wavelength zone of weakness.

288   Our findings also illustrate that the lithosphere of ice shells can support topographic loads

289   at short wavelengths. The short-wavelength scenario shows surface topography to be stable with

290   and without buoyancy, while the initially isostatic basal topography relaxes away (Figure 2a),

291   indicating that contribution of buoyancy supporting the load is insignificant and that any root

292   sticking into the ocean would flow away rapidly. The length at which lithospheric support begins

293   to decrease is contingent on the surface temperature, and potentially, the presence of antifreeze in

294   the ocean. These findings agree with Damptz and Dombard (2011), who highlighted the

295   significant role of surface temperature in controlling creep at the base of the lithosphere for the

296   moons of Jupiter and Saturn. Due to viscous creep, the lithosphere is not static. Stresses relax at

297   the base of the lithosphere, allowing the lithosphere to thin with time. Surface temperature, and

298   to a lesser degree heat flow and grain size, control creep rates.

299   It is important to note that while the surface topography at both short and long

300   wavelengths can be stable over geologic times, the basal topography exhibits distinctly different

301   behaviors at varying spatial scales. At short wavelengths, basal topography relaxes away

302   indicating topographic features at these scales are not compensated. Conversely, at long

303   wavelengths, topography at the base of the ice shell stays in isostatic equilibrium with the surface

304   topography. This finding can be attributed to the relative size of the vertical flow region and the

305   lateral extent of the topography. For long wavelengths, the vertical extent of the area where

306   material can flow laterally and redistribute is small compared to the horizontal extent (cf.

307   Stevenson, 2000). This imbalance results in a highly channelized flow that inhibits the overall

308   relaxation process observed at shorter wavelengths.

309   Moreover, when the wavelength of a load is small compared to the planetary radius, the

310   stresses caused by the body's curvature can be ignored. However, when curvature is introduced,

311   horizontal membrane stresses can contribute to the support of the surface load (Turcotte, 1981).

312   In the context of this study, membrane stresses are appreciable at approximately spherical

313   harmonic degree $l = 16$, assuming the lithosphere is ~6 km thick. This degree corresponds to a

314   wavelength of ~600 km. At this scale, topography loses just 10% of its initial height when

315   surface temperature is 100 K, and this relaxation is further reduced for colder surface

316   temperatures (Figure 2). Consequently, the inclusion of membrane stresses would reinforce our

317   findings regarding the stability of long wavelength topography.

318   To sum up, there are two competing effects for the application of Airy isostasy in an ice

319   shell over an ocean, one of which does not exist in traditional applications of Airy isostasy in

320   terrestrial worlds. First, the lithospheric strength of icy shells is a sufficient support mechanism

321   for topography at short wavelengths, without needing help from buoyancy. This finding is

322   evidenced by the "No Buoyancy" curve in Figure 2a, and it mirrors the lithospheric behavior of

323   rocky planets. In contrast, the "No Strength" curve in Figure 2a, which does not come from

324   simulations but from subtracting the "Buoyancy and Strength" and "No Buoyancy" curves and

325   thus mimics a scenario where any lithosphere would have no strength, stands in contrast to the

326   expected behavior in a terrestrial world, which would be locked at 1 at all scales. These two

327   curves – "No Buoyancy" and "No Strength" – together determine the final topographic support.

328   To understand this behavior, consider the effect of pressing one's finger into a seat

329   cushion. The cushion diffuses the stresses introduced by the force of the finger, and the opposite

330   side of the cushion is negligibly deformed, if at all. A sufficiently wide scale load, however,

331   would feel the hard seat underneath, even when pressed into the cushion at the same force per

332   unit area. Translating to ocean worlds, the seat cushion inhibits buoyant support at short

333   wavelengths, though the lithosphere can provide the support, while concurrently, the basal

334   topography can relax away without affecting the surface. At long wavelengths, the seat cushion

335   is too thin for buoyancy to be inhibited, so topography can be supported, even if the lithosphere

336   provides no support. Simultaneously at these scales, highly channelized flow precludes

337   relaxation of the basal topography. At intermediate scales, neither the seat cushion or the

338   lithosphere are fully effective, and topography cannot be supported over geologic timescales by a

339   crustal root alone, and would need another mechanism of support (e.g., Pratt). How these curves

340 add, and thus the size of the intermediate zone, is dependent on local conditions, as suggested by

341 Figure 2b. For the case of Europa explored here, this wavelength range spans over an order of

342 magnitude (from < 100 km to > 1000 km), with substantial lack of support for equatorial regions

343 where surface temperatures are higher.

344   This study begins to address the complexities of topographic support mechanisms in icy

345 shells. The results, particularly those regarding varied surface and ocean temperatures and

346 rheological conditions, offer insights into how other icy bodies might respond, and serve as a

347 foundational point for more extensive future research that could delve into a broader range of

348 parameters, including different assumptions about viscosity and rheology. Additionally, thought

349 experiments on how different conditions would affect the lithospheric thickness and the

350 thickness of the decoupling flow channel, and thus the impact on the curves in Figure 2 (such as

351 was done for the above discussion of a convective ice shell), could also provide insight on how

352 the phenomenon would play out on different ocean worlds.

5 Conclusion

354   Our results yield a more nuanced understanding of the wavelength dependence of icy

355 shell evolution, offering insights that could enhance the interpretation of topography and gravity

356 data from the icy ocean worlds. While surface topography of short-wavelength features persists

357 over geologic time, compensated roots relax away quickly. Consequently, shell thickness

358 estimates derived from short-wavelength features will not accurately represent the local

359 thickness. In contrast, long-wavelength topography could be supported by shell thickness

360 variations, such as on Titan (Nimmo and Bills, 2010). Surface topography at intermediate scales

361 is unlikely to be isostatically compensated via buoyant support.

362   The practical implications of this more complex behavior have already been revealed at

363 other icy worlds. The isolated plateaus on Titan appear to exist in the short wavelength regime,

364 being supported by the strength of Titan's lithosphere with any root relaxing away quickly,

365 suggesting top-down construction of the plateaus (Schurmeier et al., 2016). Conversely, the

366 megadome on Ganymede appears to be firmly in the intermediate regime, unable to be supported

367 by either lithospheric strength of a buoyant crustal root and implicating Pratt isostasy (Kay et al.,

368 2018).

369   Such complexities and limitations underscore the challenges inherent in applying

370   traditional isostatic models to icy shells and highlight the importance of continuous model

371   refinement. Furthermore, the importance of a nuanced understanding of the dynamics of icy

372   shells cannot be overstated, especially in the context of future space missions.

378

Open Research

380   The commercial finite element package, Marc, is available with academic pricing (Hexagon,

381   2023). Supporting information Table S2 shows the elevations of the surface and root

382   topographies, calculated from displacements, for each simulation type and wavelength (Tucker

383   & Dombard, 2023).

384

References

Airy, G. B. (1855). On the computation of the effect of the attraction of mountain-masses, as disturbing the apparent astronomical latitude of stations in geodetic surveys. *Philosophical Transactions of the Royal Society of London*, *145*, 101–104. https://doi.org/10.1098/rstl.1855.0003

Barrell, J. (1914). The Strength of the Earth's Crust. *The Journal of Geology*, *22*(8), 729–741. https://doi.org/10.1086/622189

Beuthe, M. (2021a). Isostasy with Love – I: elastic equilibrium. *Geophysical Journal International*, *225*(3), 2157–2193. https://doi.org/10.1093/gji/ggab073

Beuthe, M. (2021b). Isostasy with Love: II Airy compensation arising from viscoelastic relaxation. *Geophysical Journal International*, *227*(1), 693–716. https://doi.org/10.1093/gji/ggab241

Billings, S. E., & Kattenhorn, S. A. (2005). The great thickness debate: Ice shell thickness models for Europa and comparisons with estimates based on flexure at ridges. *Icarus*, *177*(2), 397–412. https://doi.org/10.1016/j.icarus.2005.03.013

Čadek, O., Souček, O., & Běhounková, M. (2019a). Is Airy Isostasy Applicable to Icy Moons? *Geophysical Research Letters*, *46*(24), 14299–14306. https://doi.org/10.1029/2019GL085903

Čadek, O., Souček, O., Běhounková, M., Choblet, G., Tobie, G., & Hron, J. (2019b). Long-term stability of Enceladus' uneven ice shell. *Icarus*, *319*(May 2018), 476–484. https://doi.org/10.1016/j.icarus.2018.10.003

Damptz, A. L., & Dombard, A. J. (2011). Time-dependent flexure of the lithospheres on the icy satellites of Jupiter and Saturn. *Icarus*, *216*(1), 86–88. https://doi.org/10.1016/j.icarus.2011.07.011

Dahlen, F. A. (1982). Isostatic geoid anomalies on a sphere. *Journal of Geophysical Research*, *87*(B5), 3943. https://doi.org/10.1029/JB087iB05p03943

Daly, R. A. (1940). *Strength and structure of the Earth*. Hinds, N. (Ed.). New York, NY: Prentice-Hall.

Dombard, A. J., Johnson, C. L., Richards, M. A., & Solomon, S. C. (2007). A magmatic loading model for coronae on Venus. *Journal of Geophysical Research*, *112*(4), 1–13. https://doi.org/10.1029/2006JE002731

Dombard, A. J., & McKinnon, W. B. (2000). Long-term retention of impact crater topography on Ganymede. *Geophysical Research Letters*, *27*(22), 3663–3666. https://doi.org/10.1029/2000GL011695

Dombard, A. J., & McKinnon, W. B. (2006a). Elastoviscoplastic relaxation of impact crater topography with application to Ganymede and Callisto. *Journal of Geophysical Research: Planets*, *111*(1), 1–22. https://doi.org/10.1029/2005JE002445

Dombard, A. J., & McKinnon, W. B. (2006b). Folding of Europa's icy lithosphere: an analysis of viscous-plastic buckling and subsequent topographic relaxation. *Journal of Structural Geology*, *28*(12), 2259–2269. https://doi.org/10.1016/j.jsg.2005.12.003

Durham, W. B., Prieto-Ballesteros, O., Goldsby, D. L., & Kargel, J. S. (2010). Rheological and Thermal Properties of Icy Materials. *Space Science Reviews*, *153*(1–4), 273–298. https://doi.org/10.1007/s11214-009-9619-1

Durham, W. B., & Stern, L. A. (2001). Rheological properties of water ice—Applications to satellites of the outer planets. *Annual Review of Earth and Planetary Sciences*, *29*(1), 295–330. https://doi.org/10.1146/annurev.earth.29.1.295

Gammon, P. H., Kiefte, H., & Clouter, M. J. (1983). Elastic constants of ice samples by Brillouin spectroscopy. *The Journal of Physical Chemistry*, *87*(21), 4025–4029. https://doi.org/10.1021/j100244a004

Goldsby, D. L., & Kohlstedt, D. L. (2001). Superplastic deformation of ice: Experimental observations. *Journal of Geophysical Research: Solid Earth*, *106*(B6), 11017–11030. https://doi.org/10.1029/2000JB900336

437   Hexagon (2023). *Marc* (Version 2022.2) [Software]. https://hexagon.com/products/marc

438   Hemingway, D. J., & Matsuyama, I. (2017). Isostatic equilibrium in spherical coordinates and
439   implications for crustal thickness on the Moon, Mars, Enceladus, and elsewhere.
440   *Geophysical Research Letters*, *44*(15), 7695–7705.
441   https://doi.org/10.1002/2017GL073334

442   Hussmann, H., Spohn, T., & Wieczerkowski, K. (2002). Thermal equilibrium states of Europa's
443   ice shell: Implications for internal ocean thickness and surface heat flow. *Icarus*, *156*(1),
444   143–151. https://doi.org/10.1006/icar.2001.6776

445   Kay, J. P., & Dombard, A. J. (2018). Formation of the bulge of Iapetus through long-wavelength
446   folding of the lithosphere. *Icarus*, *302*, 237–244.
447   https://doi.org/10.1016/j.icarus.2017.10.033

448   Kay, J. P., Schenk, P. M., Dombard, A. J., & McKinnon, W. B. (2018). The 3-km high subjovian
449   megadome on Ganymede: Simulation of stability via Pratt isostasy. In *49th Lunar and*
450   *Planetary Science Conference*.

451   McKinnon, W. B. (1999). Convective instability in Europa's floating ice shell. *Geophysical*
452   *Research Letters*, *26*(7), 951–954. https://doi.org/10.1029/1999GL900125

453   Nimmo, F., & Bills, B. G. (2010). Shell thickness variations and the long-wavelength topography
454   of Titan. *Icarus*, *208*(2), 896–904. https://doi.org/10.1016/j.icarus.2010.02.020

455   Nimmo, F., Bills, B. G., & Thomas, P. C. (2011). Geophysical implications of the long-
456   wavelength topography of the Saturnian satellites. *Journal of Geophysical Research:*
457   *Planets*, *116*(11), 1–12. https://doi.org/10.1029/2011JE003835

458   Nimmo, F., Giese, B., & Pappalardo, R. T. (2003a). Estimates of Europa's ice shell thickness
459   from elastically-supported topography. *Geophysical Research Letters*, *30*(5), 1–4.
460   https://doi.org/10.1029/2002gl016660

461   Nimmo, F., Pappalardo, R. T., & Giese, B. (2003b). On the origins of band topography, Europa.
462   *Icarus*, *166*(1), 21–32. https://doi.org/10.1016/j.icarus.2003.08.002

463   Ojakangas, G. W., & Stevenson, D. J. (1989). Thermal State of an Ice Shell on Europa. *Icarus*,
464   *81*(2), 220–241. https://doi.org/10.1016/0019-1035(89)90052-3

465   Pappalardo, R. T., Belton, M., Breneman, H. H., Carr, M. H., Chapman, C. R., Collins, G. C., et
466   al. (1999). Does Europa have a subsurface ocean? Evaluation of the geological evidence.
467   *Journal of Geophysical Research: Planets*, *104*(E10), 24015–24055.
468   https://doi.org/10.1029/1998JE000628

469   Petrenko, V. F., & Whitworth, R. W. (1999). *Physics of Ice*. *Physics of Ice*. Oxford University
470   Press. https://doi.org/10.1093/acprof:oso/9780198518945.001.0001

471   Pratt, J. H. (1855). On the attraction of the Himalaya Mountains, and of the elevated regions
472   beyond them, upon the plumb-line in India. *Philosophical Transactions of the Royal*
473   *Society of London*, *145*(2), 53–100. https://doi.org/10.1098/rstl.1855.0002

474   Prockter, L. M., Patterson, G. W. (2009). Morphology and Evolution of Europa's Ridges and
475   Bands. In R. T. Pappalardo, W. B. McKinnon, & K. K. Khurana (Eds.), *Europa* (pp. 237–
476   258). University of Arizona Press. https://doi.org/10.2307/j.ctt1xp3wdw.16

477   Ranalli, G. (1995). *Rheology of the Earth*. Chapman and Hall.

478   Schenk, P. M., & McKinnon, W. B. (2009). One-hundred-km-scale basins on Enceladus:
479   Evidence for an active ice shell. *Geophysical Research Letters*, *36*(16), 1–5.
480   https://doi.org/10.1029/2009GL039916

481   Schenk, P. M., & Pappalardo, R. T. (2004). Topographic variations in chaos on Europa:
482   Implications for diapiric formation. *Geophysical Research Letters*, *31*(16), L16703.
483   https://doi.org/10.1029/2004GL019978

484   Schmidt, B. E., Blankenship, D. D., Patterson, G. W., & Schenk, P. M. (2011). Active formation
485   of "chaos terrain" over shallow subsurface water on Europa. *Nature*, *479*(7374), 502–
486   505. https://doi.org/10.1038/nature10608

487   Schurmeier, L. R., Dombard, A. J., & Radebaugh, J. (2016). Titan's isolated mountain plateaus:
488   Investigating possible support mechanisms and cryovolcanic origins. In *47th Lunar and
489   Planetary Science Conference*.

490   Spohn, T., & Schubert, G. (2003). Oceans in the icy Galilean satellites of Jupiter? *Icarus*, *161*(2),
491   456–467. https://doi.org/10.1016/S0019-1035(02)00048-9

492   Stevenson, D. J. (2000). Limits on the variation of thickness of Europa's ice shell. In *31st Lunar
493   and Planetary Science Conference*.

494   Tobie, G., Choblet, G., & Sotin, C. (2003). Tidally heated convection: Constraints on Europa's
495   ice shell thickness. *Journal of Geophysical Research*, *108*(E11), 5124.
496   https://doi.org/10.1029/2003JE002099

497   Tucker, W. S., & Dombard, A. J. (2023) Elevation data for On the More Complex Wavelength
498   Dependency of Airy Isostasy in Icy Shells of Ocean Worlds [Data set]. Zenodo.
499   https://doi.org/10.5281/zenodo.8277281

500   Turcotte, D. L., & Schubert, G. (2014). *Geodynamics*. Cambridge University Press.

501   Turcotte, D. L., Willemann, R. J., Haxby, W. F., & Norberry, J. (1981). Role of membrane
502   stresses in the support of planetary topography. *Journal of Geophysical Research*,
503   *86*(B5), 3951–3959. https://doi.org/10.1029/JB086iB05p03951

504   Williams, K. K., & Greeley, R. (1998). Estimates of ice thickness in the Conamara Chaos Region
505   of Europa. *Geophysical Research Letters*, *25*(23), 4273–4276.
506   https://doi.org/10.1029/1998GL900144